e-ISSN 2150-5551
CN 31-2103/TB

Nano-Micro Letters

ARTICLE

https://doi.org/10.1007/s40820-026-02076-0

Cite as
Nano-Micro Lett.
(2026) 18:253

Received: 4 November 2025
Accepted: 25 December 2025

Beyond Conversion Chemistry: Unlocking a Cooperative Solid-Solution–Capacitive Sodium-Storage Mechanism in Nickel Phosphide

Jiaqin Liu[1,3] ✉, Tongzhen Wang[2], Jie Yang[2], Yulei Li[2] ✉, Zhaoqian Li[3], Jiewu Cui[2], Yan Yu[4] ✉, Yucheng Wu[2,3] ✉

HIGHLIGHTS

- A cooperative dual-mode sodium-storage mechanism, combining interstitial solid-solution intercalation and surface pseudocapacitance, is identified, diverging from the conventional conversion-dominated chemistry of nickel phosphides.
- In-situ/*ex-situ* analyses provide direct evidence of reversible Na^+ insertion into lattice interstitials through (111)-oriented interplanar channels, enabling low-strain lattice breathing without phase transformation.
- The freestanding Ni_2P composite electrode achieves exceptional performance, including high reversible capacity (≈560 mAh g^{-1}), remarkable rate capability (135 mAh g^{-1} at 10 A g^{-1}), and long-term stability over 2000 cycles.

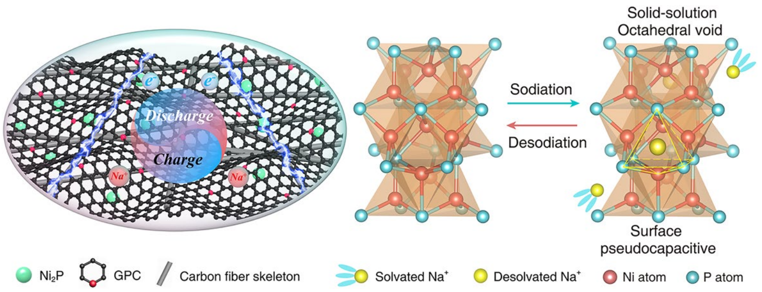

ABSTRACT Nickel-rich nickel phosphide (Ni_2P) has emerged as a promising sodium-ion battery anode owing to its high theoretical capacity and intrinsic electronic conductivity, yet its charge storage chemistry remains controversial and is often oversimplified as a conversion reaction. Herein, we design a freestanding Ni_2P composite electrode composed of ultrasmall Ni_2P nanocrystals embedded within a phosphorus-doped, graphene-like porous carbon matrix. Comprehensive in-situ and *ex-situ* analyses unequivocally demonstrate an interstitial solid-solution mechanism, wherein Na^+ ions reversibly occupy lattice interstitials via (111)-oriented interplanar channels, inducing reversible lattice breathing without phase transformation. This bulk intercalation process is synergistically coupled with a substantial pseudocapacitive contribution, establishing a cooperative dual-mode storage mechanism. Benefiting from this solid-solution–capacitive chemistry, the electrode delivers a high reversible capacity (≈560 mAh g^{-1}), outstanding rate capability (135 mAh g^{-1} at 10 A g^{-1}), and exceptional long-term stability (263 mAh g^{-1} after 2000 cycles). When paired with a $Na_3V_2(PO_4)_3$@C cathode, the full cell achieves a high-energy density of 245 Wh kg^{-1}. This work establishes solid-solution–capacitive coupling as a general paradigm for designing high-rate and durable sodium-ion battery anodes.

KEYWORDS Sodium-ion battery; Anode; Ni_2P; Solid-solution; Pseudocapacitive

---

✉ Jiaqin Liu, jqliu@buct.edu.cn; Yulei Li, lyl@hfut.edu.cn; Yan Yu, yanyumse@ustc.edu.cn; Yucheng Wu, ycwu@hfut.edu.cn
[1] State Key Laboratory of Chemical Resource Engineering, College of Chemistry, Beijing University of Chemical Technology, Beijing 100029, People's Republic of China
[2] School of Mechanical Engineering, School of Materials Science and Engineering, Engineering Research Center of Advanced Composite Materials Design & Application of Anhui Province, Hefei University of Technology, Hefei 230009, People's Republic of China
[3] School of New Energy Engineering, Hefei Institute of Technology, Hefei 238706, People's Republic of China
[4] Department of Materials Science and Engineering, CAS Key Laboratory of Materials for Energy Conversion, Hefei National Research Center for Physical Sciences at the Microscale, University of Science and Technology of China, Hefei 230026, People's Republic of China

1 Introduction

Given the pressing need for cost-effective and sustainable energy storage, sodium-ion batteries (SIBs) have emerged as a compelling post-lithium alternative, driven by the earth-abundance and low cost of sodium, and envisioned to play a pivotal role in stabilizing large-scale renewable energy grids [1–4]. However, the practical deployment of SIBs is hampered by the intrinsic characteristics of Na^+—its large ionic radius (1.02 Å) and relatively high redox potential (-2.71 V vs. SHE) relative to Li^+ (-3.04 V vs. SHE) [5, 6]. Such intrinsic features collectively result in sluggish solid-state diffusion kinetics, limited energy density, and pronounced structural instability in host materials during cycling [7–9]. Consequently, developing anode materials with rapid ion/electron transport, robust structural resilience, and high reversible capacity remains a crucial yet challenging pursuit.

Among various anode candidates, nickel-rich nickel phosphide (Ni_2P) stands out due to its distinctive bonding characteristics arising from the synergistic interplay between metallic Ni–Ni bonding and a robust covalent Ni–P framework [10, 11]. This dual bonding nature endows Ni_2P with high intrinsic electronic conductivity, structural robustness, and tunable redox properties, thereby positioning it as a promising sodium-ion battery anode, as reflected by its high theoretical capacity and advantageous operating voltages [12–15]. In particular, compared with hard carbon, the current commercial benchmark characterized by limited intrinsic conductivity, moderate capacity, and low tap density, Ni_2P provides markedly higher electronic conductivity, a substantially higher theoretical capacity, and a greater tap density conducive to enhancing volumetric energy density, underscoring its potential for high-rate and high-energy SIB applications [1, 16, 17]. Despite these advantages, the Na^+ storage chemistry of Ni_2P remains controversial. Conventionally, the prevailing model for Na^+ storage predominantly ascribes to a conversion reaction mechanism, culminating in the formation of Na_3P and metallic Ni [18–20]. However, recent in-situ and operando characterizations have repeatedly failed to identify these expected crystalline products, revealing a clear inconsistency with the conventional mechanism and highlighting a critical gap in our mechanistic understanding of Na^+ storage in Ni_2P [21].

At the nanoscale, however, sodium-storage mechanisms are governed by distinct thermodynamic and kinetic constraints that deviate markedly from bulk behavior [22–24]. When the particle size is reduced below a critical threshold (~ 20 nm), the enlarged surface-to-volume ratio and elevated nucleation barrier suppress classical conversion reactions [25], giving rise instead to an interstitial solid-solution–type process complemented by a surface redox pseudocapacitive contribution [26–29]. This cooperative intercalation–capacitive mechanism has been documented in several transition-metal chalcogenides [30–33]. However, whether a similar mechanism operates in transition-metal phosphides (TMPs) such as Ni_2P remains unclear, largely owing to the lack of direct in-situ structural or spectroscopic evidence.

In this work, we resolve the long-standing mechanistic ambiguity of Ni_2P by constructing a hierarchical, freestanding Ni_2P@GPC/CFP composite electrode, integrating ultrasmall Ni_2P nanocrystals into a graphene-like phosphorus-doped carbon (GPC) matrix on a carbon fiber paper (CFP) scaffold. This composite electrode serves as both a high-performance anode and a platform for mechanistic exploration. In-situ X-ray diffraction, quasi-insitu X-ray photoelectron spectroscopy, and density functional theory analyses collectively uncover a cooperative sodium-storage mechanism, in which Na^+ ions reversibly access interstitial sites through (111)-oriented interplanar channels, inducing low-strain lattice breathing without phase transformation. A concurrent pseudocapacitive process further accelerates charge-storage kinetics. This conversion-free, dual-mode solid-solution–capacitive behavior redefines the sodium-storage mechanism in Ni_2P and establishes a generalizable design principle for high-rate and durable transition-metal phosphide anodes.

2 Experimental Section

2.1 Materials

Carbon fiber paper (CFP) was obtained from Cetech Co., Ltd. Nickel acetate ($Ni(CH_3COO)_2$), glucose ($C_6H_{12}O_6$), potassium hydroxide (KOH), red phosphorus (P), sulfuric acid (H_2SO_4, ≥ 98 wt%), hydrochloric acid (HCl, 35 wt%), nitric acid (HNO_3, ≥ 65 wt%), oxalic acid dihydrate ($C_2H_2O_4 \cdot 2H_2O$), sodium dihydrogen phosphate dihydrate ($NaH_2PO_4 \cdot 2H_2O$), n-propanol (C_3H_6OH), sodium (Na) metal, super P, polyvinylidene fluoride (PVDF), and N-methyl-2-pyrrolidone (NMP)

https://doi.org/10.1007/s40820-026-02076-0

were purchased from Sinopharm Chemical Reagent Co., Ltd. (China). Vanadium pentoxide (V_2O_5) was obtained from Xiya Chemical Co., Ltd. GF/D glass microfiber membrane, sodium perchlorate ($NaClO_4$), ethylene carbonate (EC), dimethyl carbonate (DMC), fluoroethylene carbonate (FEC), and aluminum (Al) foil were purchased from the DoDoChem. Argon (Ar) and Ar/H_2 (9:1, v/v) were supplied by Hefei Kexun Chemical Co., Ltd.

2.2 Synthesis of Ni_2P@GPC/CFP Composite

To synthesize the Ni_2P@GPC/CFP composite, 4 mmol of nickel acetate and 5.5 mmol of glucose were dissolved in 50 mL deionized water under magnetic stirring. Subsequently, 50 mL of 1.5 M KOH solution was added dropwise, followed by continuous stirring at room temperature for 6 h. Then, 6 mmol of red phosphorus was added, and the mixture was stirred for an additional 12 h. The resulting mixture was heated to 80 °C to partially evaporate the solvent, yielding a viscous precursor slurry.

The precursor slurry was uniformly coated onto CFP (areal density: 2.0 mg cm^{-2}) and dried under vacuum at 60 °C for 12 h, resulting in an areal precursor mass loading of 3–5 mg cm^{-2}. The coated CFP was subsequently annealed at 850 °C for 4 h under an Ar atmosphere at a heating rate of 3 °C min^{-1}. The annealed product was sequentially washed with 1 M HCl and deionized water, and then dried under vacuum at 60 °C for 24 h to obtain the final Ni_2P@GPC/CFP composite. The mass loading of the active Ni_2P@GPC was 1.4 ± 0.2 mg cm^{-2}.

2.3 Synthesis of GPC/CFP and Ni_2P

The GPC/CFP composite was obtained by selectively removing Ni_2P from the Ni_2P@GPC/CFP electrode through aqua regia etching, followed by thorough rinsing with deionized water and drying. For comparison, pure Ni_2P was synthesized using the same protocol as Ni_2P@GPC/CFP, except that glucose and the CFP substrate were omitted.

2.4 Synthesis of $Na_3V_2(PO_4)_3$@C (NVP@C) Composite

In a typical process, 3.95 mmol of V_2O_5 and 12 mmol of $C_2H_2O_4 \cdot 2H_2O$ were dissolved in 40 mL of deionized water under stirring at 70 °C for 1 h to form a light-blue solution. Subsequently, 11.8 mmol of $NaH_2PO_4 \cdot 2H_2O$ and 2.2 mmol of glucose were added and stirred for 30 min. Then, 100 mL of n-propanol was added, followed by stirring for an additional hour. The resulting mixture was dried at 90 °C for 6 h to yield a solid precursor.

The dried precursor was ground into a fine powder and subjected to a two-step thermal treatment under an Ar/H_2 (9:1, v/v) atmosphere: preheating at 350 °C for 4 h at a heating rate of 2 °C min^{-1}, followed by calcination at 800 °C for 6 h at a heating rate of 5 °C min^{-1}, yielding the final NVP@C composite as a black powder.

2.5 Materials Characterization

X-ray diffraction (XRD, D/Max-2500 V, Rigaku) with $Cu_{K\alpha}$ radiation ($\lambda = 0.154056$ nm) was used to identify the crystalline phases, with scanning performed over $2\theta = 10°$-$80°$ at a scan rate of 5° min^{-1}. The morphology and microstructure were examined using field-emission scanning electron microscopy (FE-SEM, ZEISS Sigma 300) and field-emission transmission electron microscopy (FE-TEM, Talos F200X G2). Elemental composition and distribution were characterized by energy-dispersive X-ray spectroscopy (EDS, Oxford Instruments, Max50). Surface chemical states were analyzed using X-ray photoelectron spectroscopy (XPS, ESCALAB 250Xi, Thermo Scientific). Raman spectroscopy (LabRAM HR Evolution, Horiba) with a 532-nm excitation laser was used to probe structural features and bonding characteristics.

Thermal stability was evaluated by thermogravimetric analysis (TGA, PerkinElmer) conducted in air from 30 to 800 °C at a heating rate of 10 °C min^{-1}. Specific surface area and pore structure were measured by Brunauer–Emmett–Teller (BET) analysis (Autosorb-IQ3).

2.6 Cell Assembly and Electrochemical Measurements

CR2032-type coin cells were assembled in an Ar-filled glovebox to evaluate the electrochemical performance of Ni_2P@GPC/CFP and GPC/CFP. These materials were directly used as working electrodes (12 mm in diameter), with sodium metal as the counter electrode, GF/D glass microfiber membrane as the separator, and 1 M $NaClO_4$ in EC/DMC (1:1, v/v) containing 5 wt% FEC as the electrolyte.

The amount of electrolyte was controlled at 180 µL per cell. Galvanostatic cycling was performed within 0.01–3.0 V (vs. Na^+/Na).

In-situ XRD measurements were carried out using a specially designed coin-cell configuration. The in-situ cell was assembled following the same procedure as the half-cell, except that the stainless-steel cathode cap was replaced by a Be window to allow X-ray penetration, whereas the anode cap was replaced by a sealed steel sleeve. The assembled cell was mounted onto the XRD stage with the Be window facing the X-ray beam, and electrical leads were connected to an electrochemical workstation. During the measurement, XRD patterns were continuously collected over $2\theta = 30°$-$60°$ at a scan rate of 5° min^{-1}, while the cell was cycled at 50 mA g^{-1} within 0.01–3.0 V (vs. Na^+/Na).

For the preparation of Ni_2P electrodes, a slurry of Ni_2P, Super P, and polyvinylidene fluoride (PVDF) (8:1:1, w/w) in N-methyl-2-pyrrolidone (NMP) was cast onto Al foil and dried under vacuum at 60 °C for 12 h. Circular disks (12 mm diameter) with an active-material mass loading of 1.4–1.6 mg cm^{-2} were punched and assembled into half-cells under the same conditions described above.

For full-cell testing, the NVP@C cathode was prepared following the same casting procedure. The areal mass loadings of the cathode and anode were controlled at a ratio of 2:1, with the cathode loading fixed at 3.0 mg cm^{-2}. Prior to full-cell assembly, the Ni_2P@GPC/CFP anode was activated at 50 mA g^{-1} for 5 cycles within 0.01–3 V (vs. Na^+/Na). Full cells were assembled using Ni_2P@GPC/CFP as the anode and NVP@C as the cathode, and cycled within 0.5–3.7 V. The energy and power densities were calculated using the following equations [34, 35]:

$$E = \frac{I\Delta t\Delta V}{3.6m} \quad (\mathrm{Wh\ kg^{-1}}) \tag{1}$$

$$P = \frac{3600E}{\Delta t} \quad (\mathrm{W\ kg^{-1}}) \tag{2}$$

where I (A) is the discharge current, Δt (s) is the discharge time, ΔV (V) is the average voltage, and m (g) is the total mass of active materials on both electrodes.

Galvanostatic charge–discharge (GCD) and galvanostatic intermittent titration technique (GITT) tests were conducted on a Neware battery testing system. Cyclic voltammetry (CV) and electrochemical impedance spectroscopy (EIS) measurements were performed on an Autolab PGSTAT302N electrochemical workstation. EIS was carried out over a frequency range of 10 mHz to 100 kHz with an amplitude of 5 mV. CV scans were recorded within 0.01–3.0 V at a scan rate of 0.1 mV s^{-1}. GITT was applied to estimate the Na^+ diffusion coefficient. The half-cells were discharged within 0.01–3 V at 50 mA g^{-1} for a 20 min current pulse, followed by a 2-h relaxation period. This pulse-rest sequence was repeated until the cutoff voltage was reached. For EIS analysis, the Warburg coefficient (σ_w) was extracted from the linear relationship between the real part of impedance (Z') and $\omega^{-0.5}$ in the low-frequency region ($\omega = 2\pi f$). The Na^+ diffusion coefficient (D_{Na^+}) was calculated using the following equations [36]:

$$Z' = R_e + R_{ct} + \sigma_w \omega^{-0.5} \tag{3}$$

$$D_{Na^+} = R^2T^2/2A^2n^4F^4C^2\sigma_w^2 \tag{4}$$

where R is the gas constant, T is the absolute temperature, A is the electrode surface area, n is the number of electrons, F is the Faraday constant, and C is the molar concentration of Na^+ in the electrolyte. All electrochemical measurements were carried out at an ambient temperature of 25 °C.

2.7 Theoretical Calculations

Density functional theory (DFT) calculations were performed using the Vienna *Ab* initio Simulation Package (VASP 5.4) [37, 38]. The Perdew–Burke–Ernzerhof (PBE) functional within the generalized gradient approximation (GGA) was employed to describe electron exchange-correlation interactions, and spin polarization was included throughout the calculations [39].

A plane-wave cutoff energy of 550 eV was used. Brillouin-zone sampling was performed using a Monkhorst–Pack *k*-point mesh of $3 \times 3 \times 1$. The convergence criteria were set to 10^{-5} eV for the total energy and 0.03 eV Å^{-1} for the atomic forces. Surface models of graphene-like carbon (GC), graphene-like phosphorus-doped carbon (GPC), and $Ni_2P(111)$ were constructed using a slab geometry, in which the bottom layers were fixed, while the remaining layers were fully relaxed. A vacuum layer of 10 Å was applied along the z-axis to avoid interactions between adjacent periodic images.

The adsorption energies (E_{ad}) of a Na atom on the GC (001), GPC (001), and Ni_2P (111) surfaces were calculated using:

https://doi.org/10.1007/s40820-026-02076-0

$$E_{ad} = E_{Na@Slab} - (E_{Slab} + 1/2E_{Na}) \tag{5}$$

where $E_{Na@Slab}$ is the total energy of a Na atom adsorbed on the surface, E_{Slab} is the total energy of the pristine surface, and E_{Na} is the energy of bulk metallic sodium per unit cell (containing two Na atoms).

3 Results and Discussion

3.1 Microstructure and Structural Characterization

The Ni_2P@GPC/CFP composite was synthesized via a synchronous calcination–phosphorization strategy, during which nickel acetate was partially reduced to metallic Ni to catalyze the graphitization of the carbon precursor [40], while red phosphorus served both as a phosphorus source and a reactive modulating agent to tailor the carbon framework [41, 42]. Meanwhile, KOH activation generated abundant hierarchical porosity [43, 44], ultimately yielding a graphene-like, phosphorus-doped carbon network intimately integrated with Ni_2P nanocrystals (Fig. 1a). X-ray diffraction (XRD) patterns (Fig. 1b) verify the successful formation of crystalline Ni_2P together with a characteristic graphitic (002) reflection [45], with sharp peaks indexed to the (111), (201), (210), (300), (211), (310), (311), and (400) planes of Ni_2P (PDF 03-0953). After aqua regia etching, only the carbon (002) peak remains, unambiguously confirming that the Ni_2P phase is embedded within and stabilized by the porous carbon matrix. Scanning electron microscopy (SEM) images (Figs. 1c, d, and S1, S2) show that the Ni_2P@GPC uniformly covers the carbon fiber paper (CFP, fiber diameter ~ 10 µm; thickness ~ 230 µm), forming a freestanding three-dimensional conductive network. The CFP scaffold serves simultaneously as current collector and mechanical backbone, eliminating the need for polymer binders, conductive additives, and metal foils. This binder-free architecture simplifies electrode fabrication and significantly enhances volumetric energy density by minimizing inactive components and improving the utilization of electroactive materials. Remarkably, the Ni_2P@GPC/CFP composite maintains excellent mechanical integrity even under a 500-g load (Fig. S3), demonstrating its robustness for direct use as a SIB anode. Energy-dispersive X-ray spectroscopy (EDX) mapping (Figs. 1e and S4) demonstrates the homogeneous distribution of Ni and P within the graphene-like carbon matrix. Transmission electron microscopy (TEM) (Figs. 1f and S5, S6) further reveals an ultrathin, graphene-like porous carbon architecture that provides fast electron/ion transport pathways while offering nanoscale confinement for Ni_2P domains, which is critical for accommodating volume fluctuations during cycling. High-resolution TEM (HRTEM) images and selected area electron diffraction (SAED) patterns (Fig. 1g-i) display well-defined lattice fringes corresponding to the Ni_2P (111) and (201) planes [46], consistent with the XRD results and confirming the high crystallinity of the embedded Ni_2P nanocrystals.

X-ray photoelectron spectroscopy (XPS) further elucidates the chemical environment of the composite (Fig. S7a). The C 1*s* spectrum displays characteristic peaks assigned to C–C/C = C (284.7 eV), C-O/C-P (285.5 eV), and C =O (288.4 eV) [47–50] (Fig. S7b). The P 2*p* spectrum shows P-Ni (130.5 and 129.7 eV) and P–C (133.8 eV) signals, confirming both the formation of Ni_2P and P doping in the GPC [51, 52] (Fig. 1j). The Ni 2*p* spectrum exhibits Ni^{2+} features at 856.9 and 874.7 eV together with pronounced satellite peaks (Fig. 1k), indicative of surface oxidation and interfacial Ni–P–C interactions, which may facilitate interfacial charge transfer [53]. Raman spectra reveal distinct D and G bands at 1354 and 1590 cm^{-1} with nearly identical I_D/I_G ratios (1.06 vs. 1.05) for Ni_2P@GPC/CFP and GPC/CFP, suggesting comparable defect densities and increased surface reactivity resulting from P doping [54] (Fig. 1l). Thermogravimetric analysis (TGA) shows a major weight loss between 140 and 430 °C due to the carbon combustion and Ni_2P decomposition, followed by the formation of $Ni_3(PO_4)_2$, $Ni_2P_2O_7$, and NiO at temperatures above 585 °C [55]. Based on the residual mass, the Ni_2P content is estimated to be ~ 43.9 wt% (Fig. S7c). Nitrogen adsorption–desorption isotherms exhibit typical type-IV profiles with BET surface area of 221.0 m^2 g^{-1} and pore volume of 0.412 cm^3 g^{-1} for Ni_2P@GPC/CFP, slightly lower than that of GPC/CFP owing to the incorporation of Ni_2P nanoparticles (Fig. S7d–f). The resulting hierarchical porosity ensures efficient electrolyte infiltration and ion diffusion, thereby supporting fast electrochemical kinetics.

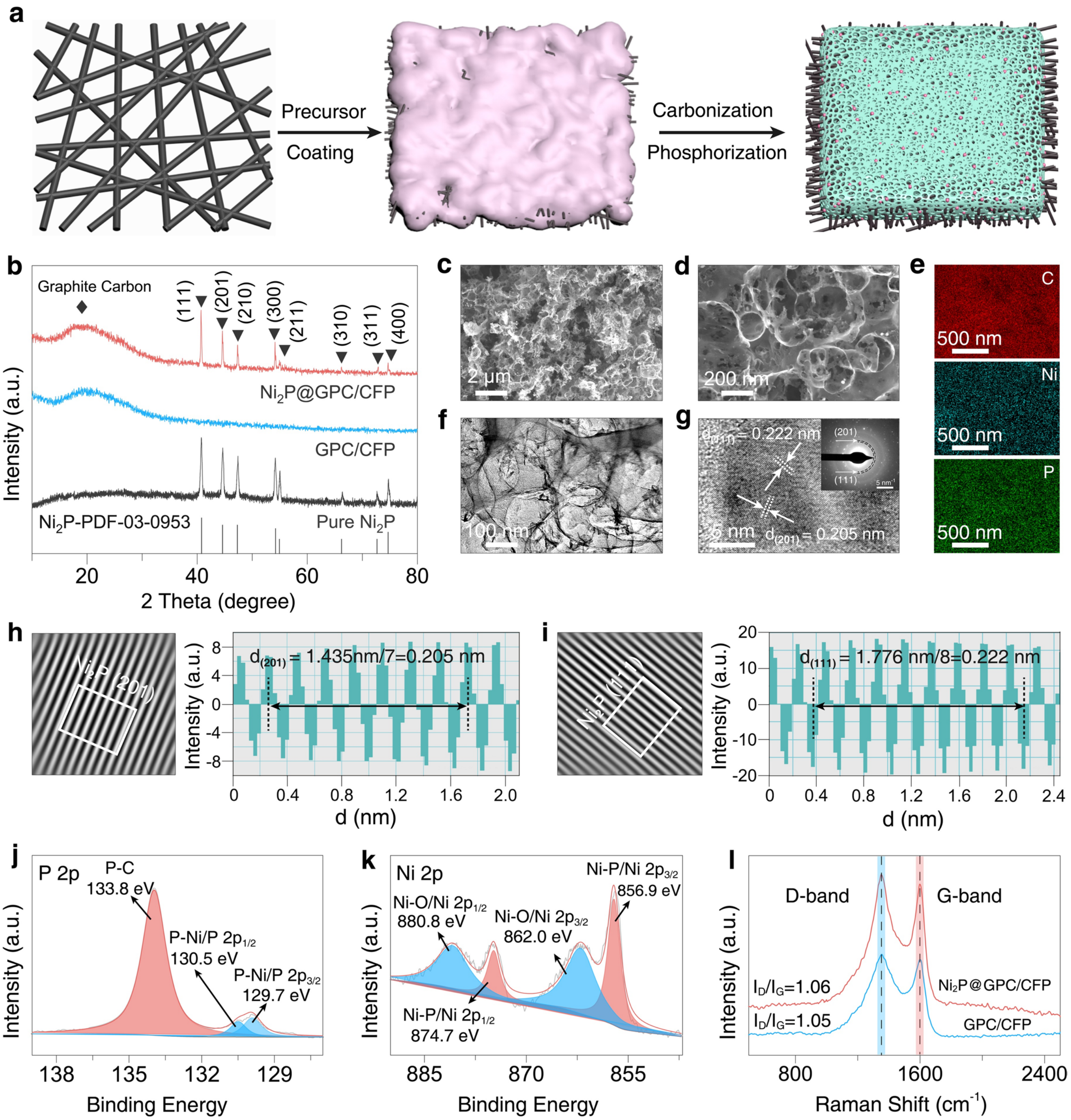

Fig. 1 **a** Schematic illustration of the synthesis for Ni_2P@GPC/CFP. **b** XRD patterns of Ni_2P@GPC/CFP, GPC/CFP, and pure Ni_2P. **c, d** SEM images and **e** corresponding EDX elemental mapping of Ni_2P@GPC/CFP matched with **d**. **f** TEM and **g** HRTEM images of Ni_2P@GPC/CFP (inset: SAED pattern). **h, i** FFT of Ni_2P. **j** P 2*p* and **k** Ni 2*p* XPS spectra of Ni_2P@GPC/CFP. **l** Raman spectra of Ni_2P@GPC/CFP and GPC/CFP

3.2 Electrochemical Performance Evaluation

The Na^+ storage performance of Ni_2P@GPC/CFP was first evaluated by CV and GCD analyses. As shown in Fig. 2a, the CV profiles at 0.1 mV s^{-1} display a broad irreversible cathodic peak at ≈2.07 V in the first scan, associated with SEI formation and electrolyte degradation [56, 57]. The cathodic peak at ≈0.91 V shifts positively to ≈0.99 V in subsequent cycles, indicative of electrode activation with reduced polarization and improved

Na^+ insertion kinetics [47, 58]. A distinct anodic peak at 1.78 V is associated with Na^+ extraction, and the highly overlapped profiles from the 2nd to 5th cycles confirm excellent reversibility. GCD measurements at 0.1 A g^{-1} show first-cycle discharge/charge capacities of 791/560 mAh g^{-1}, giving an initial Coulombic efficiency (ICE) of 70.8% (Fig. 2b). The relatively low ICE is attributed to irreversible Na^+ consumption during SEI formation and ion trapping [59]. Upon prolonged cycling, the capacity stabilizes at ≈405 mAh g^{-1} after 300 cycles, with a Coulombic efficiency (CE) of ≈99.8% and a remarkably low decay rate of ≈0.09% per cycle. The nearly identical GCD profiles (Fig. S8a) corroborate the structural integrity of the electrode. In contrast, control electrodes exhibit substantially inferior performance: GPC/CFP delivers only 148 mAh g^{-1} initially and fades to 93 mAh g^{-1} after 300 cycles, while bare Ni_2P undergoes rapid capacity loss

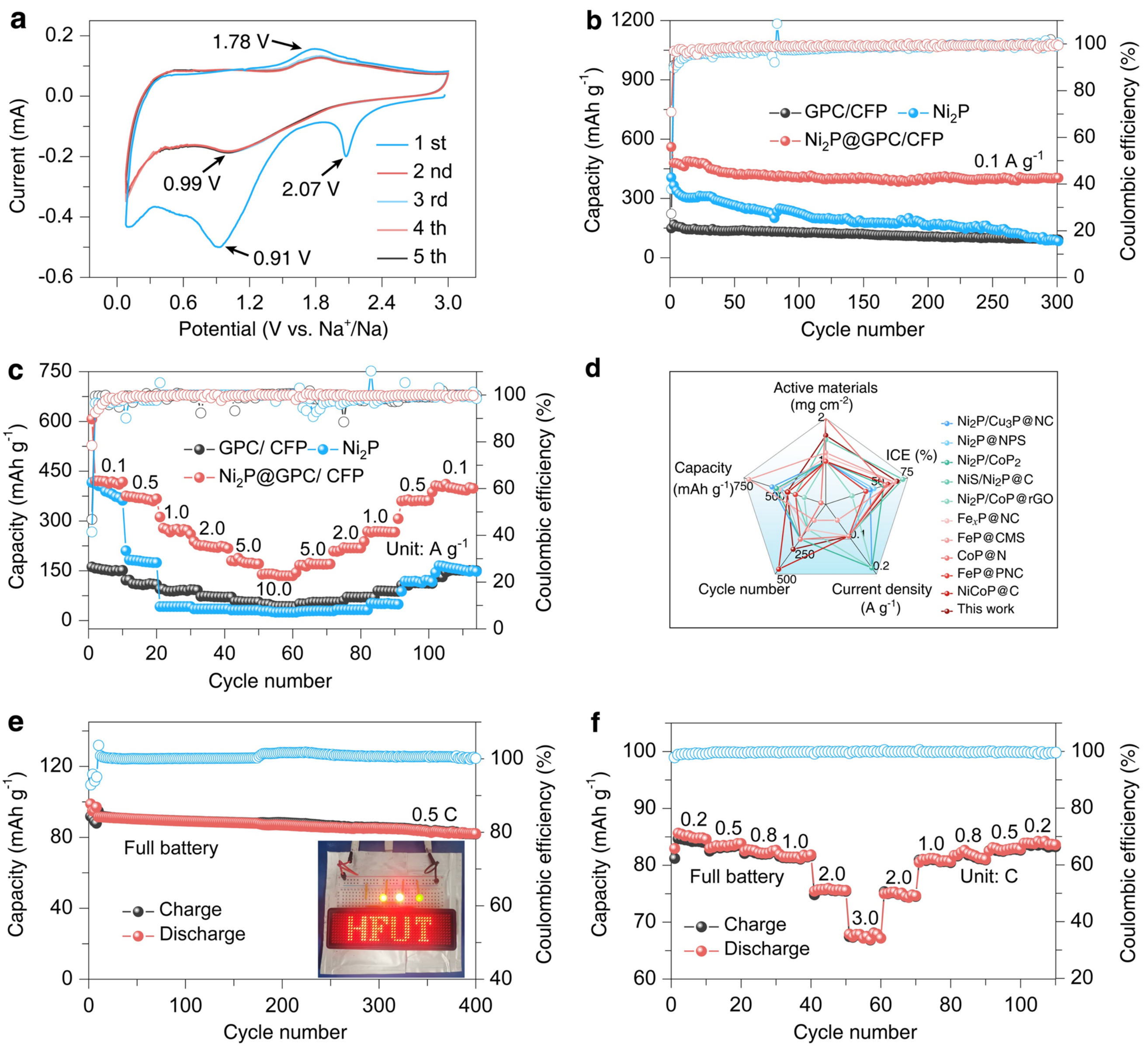

Fig. 2 **a** CV curves of Ni_2P@GPC/CFP at 0.1 mV s^{-1} for the first five cycles. **b** Cycling performance of Ni_2P@GPC/CFP, GPC/CFP, and Ni_2P at 100 mA g^{-1}. **c** Rate performance of Ni_2P@GPC/CFP, GPC/CFP, and Ni_2P. **d** Performance comparison of the Ni_2P@PC/CFP anode with previously reported transition-metal-phosphide anodes. **e** Cycling performance and **f** rate capability of Ni_2P@GPC/CFP||NVP@C full cell

due to severe pulverization and electrical disconnection (Figs. 2b and S8c, e).

At high current density (1 A g^{-1}), Ni_2P@GPC/CFP retains 263 mAh g^{-1} after 2000 cycles (78.2% retention, decay ≈ 0.02% per cycle), far outperforming GPC/CFP (79 mAh g^{-1}) and Ni_2P (50 mAh g^{-1}) (Fig. S8g). Even at an ultrahigh rate of 10 A g^{-1}, it delivers 135 mAh g^{-1}, significantly exceeding GPC/CFP and Ni_2P, and fully recovers to 396 mAh g^{-1} when the current density returns to 0.1 A g^{-1} (Figs. 2c and S8b, d, f), demonstrating outstanding rate capability. Benchmarking against state-of-the-art transition-metal-phosphide anodes (Fig. 2d; Table S1) shows that Ni_2P@GPC/CFP exhibits competitive overall performance.

To assess practical applicability, a full cell was assembled using Ni_2P@GPC/CFP as the anode and NVP@C as the cathode. The full cell delivers an initial capacity of 98 mAh g^{-1} at 0.5 C, corresponding to an energy density of 245 Wh kg^{-1} at a power density of 98 W kg^{-1} (based on the total mass of active materials in both electrodes). Remarkably, it retains 82 mAh g^{-1} after 400 cycles at 0.5 C, with a low fading rate of only 0.03% per cycle and a nearly 100% CE (Figs. 2e and S9a). The cell also exhibits robust rate performance, delivering 86 to 68 mAh g^{-1} from 0.2 to 3.0 C, with full recovery to ~ 84 mAh g^{-1} once the current density returns to 0.2 C (Figs.2f and S9b). Even at 2 C, 73 mAh g^{-1} is maintained after 400 cycles (89.3% retention; Fig. S9c, d). The ability of the assembled device to stably power an LED display (inset, Fig. 2e) visually demonstrates its practical applicability.

Ex-situ FE-SEM and EDX analyses after long-term cycling (Figs. S10–S12) reveal a well-preserved porous architecture with uniformly distributed Ni, P, and C, confirming the absence of pulverization or aggregation. This structural robustness stems from the rational material design: hierarchical porosity ensures electrolyte accessibility; the graphene-like carbon scaffold buffers volume fluctuations and maintains electrical conductivity; nanosized Ni_2P domains shorten diffusion paths and enhance interfacial kinetics; P doping improves electronic/ionic transport and provides additional active sites; and the binder-free configuration maximizes active-material utilization and minimizes interfacial side reactions, thereby offering a clean platform to probe the intrinsic Na-storage mechanism of Ni_2P.

3.3 Elucidation of Sodium-Storage Kinetics

To gain deeper mechanistic insight, the Na^+ storage kinetics were investigated using the GITT (Figs. 3a and S13a–c). According to Fick's second law [60], the Na^+ diffusion coefficient (D_{Na^+}) can be estimated as: $D_{Na^+} = \frac{4}{\pi\tau}\left(\frac{m_B V_m}{M_B S}\right)^2\left(\frac{\Delta E_s}{\Delta E_\tau}\right)^2$, where S (cm^2) is the effective electrode area; M_B (g mol^{-1}), V_m (cm^3 mol^{-1}), and m_B (g) denote the molar mass, molar volume, and mass of the active material, respectively; τ is the pulse duration; ΔE_s (V) is the steady-state voltage change, and ΔE_τ (V) is the transient voltage change during the pulse. The average $\log(D_{Na^+})$ values of -10.6, -11.0, and -11.3 (Fig. 3b) for Ni_2P@GPC/CFP, GPC/CFP, and Ni_2P highlight the enhanced Na^+ diffusivity in the composite. Nyquist plots at various discharge depths (Fig. 3c) show a consistently low and nearly invariant charge-transfer resistance (~ 10.3 Ω), with minor changes in the Warburg slope, indicative of pseudocapacitive-dominated behavior [32, 61]. For Ni_2P@GPC/CFP||Na, the interfacial resistance increases modestly after 100 cycles due to gradual SEI growth, yet it remains significantly lower than that of Ni_2P (Fig. S13d-f; Table S2), indicating that 3D hierarchical GPC framework enhances charge-transfer dynamics and stabilizes the interface during cycling. Furthermore, the Na^+ diffusion coefficients extracted from the Warburg region of the EIS spectra further corroborate the improved ion transport in Ni_2P@GPC/CFP. Compared to GPC/CFP and pure Ni_2P, Ni_2P@GPC/CFP shows consistently higher Na^+ diffusion coefficients (Figs. 3d and S13g-h; Table S2), confirming its superior ion transport properties.

To probe the charge-storage mechanism, scan rate-dependent CV analysis of Ni_2P@GPC/CFP performed (Fig. 3e). The current response (i) scales with the scan rate (v) according to a power-law ($i = av^b$) [62, 63], where a is a variable parameter, and b is an index used to assess the reaction kinetics. The b value close to 1.0 typically corresponds to surface capacitive behavior, while a value closer to 0.5 indicates a diffusion-dominated process. The b-values for oxidation (0.783) and reduction (0.755) suggest a hybrid diffusion-capacitive mechanism that enables fast Na^+ uptake and release (Fig. S14a). Quantitative deconvolution using $i = k_1\nu + k_2\nu^{1/2}$ reveals that the capacitive contribution dominates at higher scan rates [64, 65], increasing from 48.2% at

https://doi.org/10.1007/s40820-026-02076-0

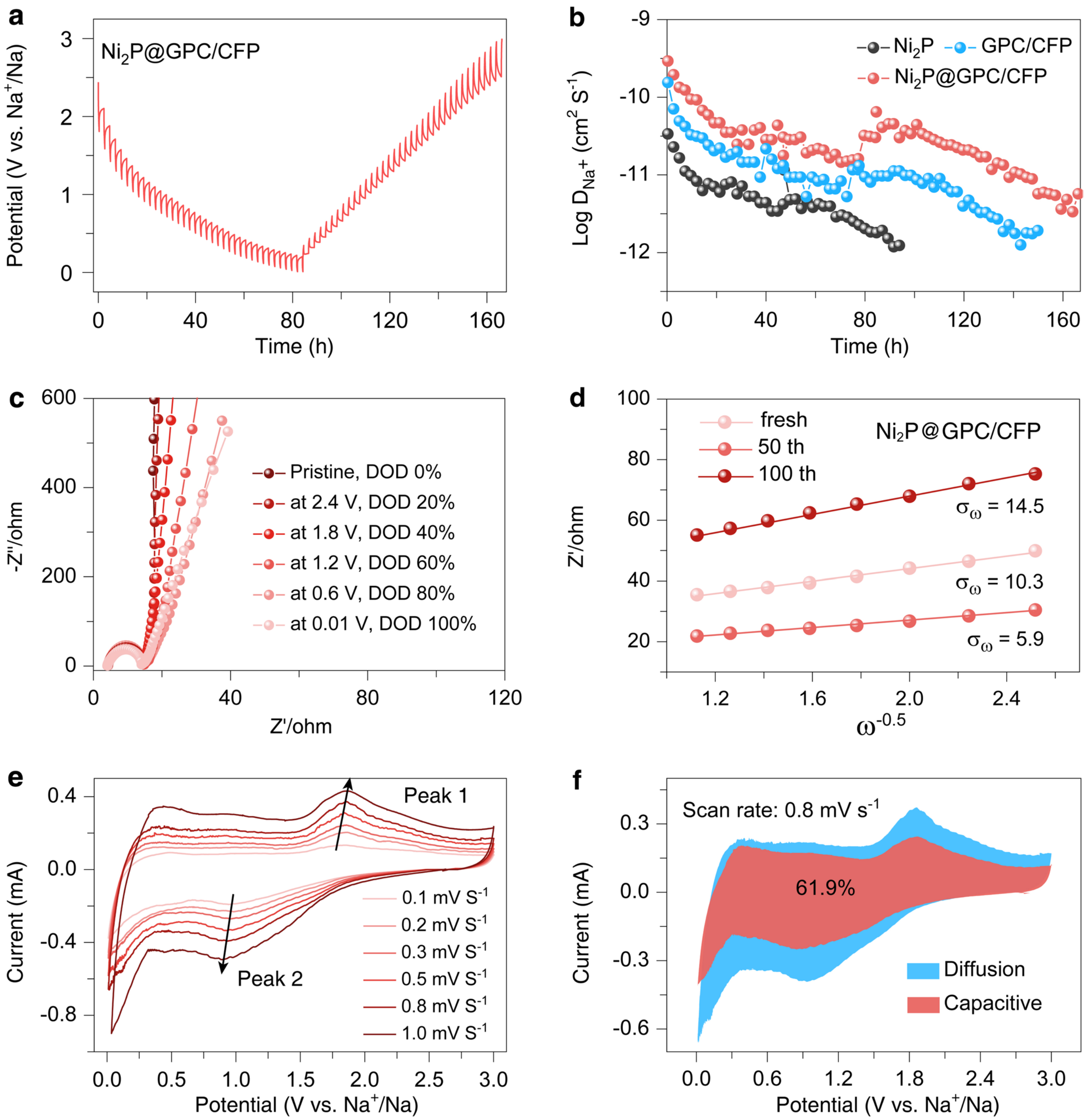

Fig. 3 **a** GITT time-potential profiles of Ni_2P@GPC/CFP. **b** Ion diffusion coefficients of Ni_2P@GPC/CFP, GPC/CFP, and Ni_2P. **c** Nyquist plots of Ni_2P@GPC/CFP at different DOD states (0.01–3.0V). **d** Fitting line of Z′ vs. $\omega^{-0.5}$ for EIS before cycling, after 50 and 100 cycles of Ni_2P@GPC/CFP. **e** CV profiles of Ni_2P@GPC/CFP at different scan rates, and **f** Capacitive-controlled contribution of Na^+ at 0.8 mV s^{-1}

0.1 mV s^{-1} to 75.4% at 1.0 mV s^{-1}, and reaching 61.9% at 0.8 mV s^{-1} (Figs. 3f and S14b). The predominance of capacitive contributions facilitates fast Na^+ uptake/release, which underpins the outstanding high-rate capability and structural durability of Ni_2P@GPC/CFP over prolonged cycling.

3.4 Mechanistic Investigation and Theoretical Validation

The Na-storage mechanism was further elucidated through a combination of in-situ/ex-situ characterizations and DFT calculations. In-situ XRD measurements during both the first and 10th cycles (Fig. 4a, e) reveal that Ni_2P@GPC/CFP retains its crystalline structure throughout sodiation and desodiation, with no appearance of new peaks, thus excluding a conversion-based process. Notably, the Ni_2P (111) reflection undergoes a fully reversible shift toward lower 2θ during sodiation and recovers upon desodiation, corresponding to a reversible unit-cell expansion of ~ 2.5% to 2.7% (Fig. 4b, f), indicating the lattice breathing behavior. The interplanar spacing of the Ni_2P (111) plane (0.220 nm) is significantly larger than the effective size of desolvated Na^+ (~ 0.102 nm), whereas other low-index planes have substantially smaller spacings. As a result, Na^+ insertion is geometrically favored along the (111)-oriented interplanar channels, enabling preferential Na^+ occupation of lattice interstitial sites (e.g., irregular octahedral voids) in Ni_2P.

Ex-situ HRTEM further corroborates this behavior: the (111) lattice spacing expands from ~ 0.220 to ~ 0.226 nm upon discharging to 0.01 V, and contracts back to ~ 0.220 nm after charging to 3.0 V during the first cycle (Fig. 4c, d). A similar trend is observed in the 10th cycle (0.228 → 0.221 nm; Fig. 4g, h). This reversible lattice breathing behavior, sustained across multiple cycles, underscores the low-strain, non-conversion nature of the interstitial solid-solution mechanism in Ni_2P. Further analysis of in-situ XRD data (Fig. S15) confirms the preservation of the crystallographic integrity of Ni_2P throughout cycling, evidenced by minimal changes in the intensity ratios of Ni_2P (201)/BeO (100) and Ni_2P (210)/BeO (100). Long-term *ex-situ* XRD (Fig. S16) reveals that the (111) peak continues to shift to lower angles during sodiation, but the extent of this shift progressively decreases and stabilizes, suggesting that

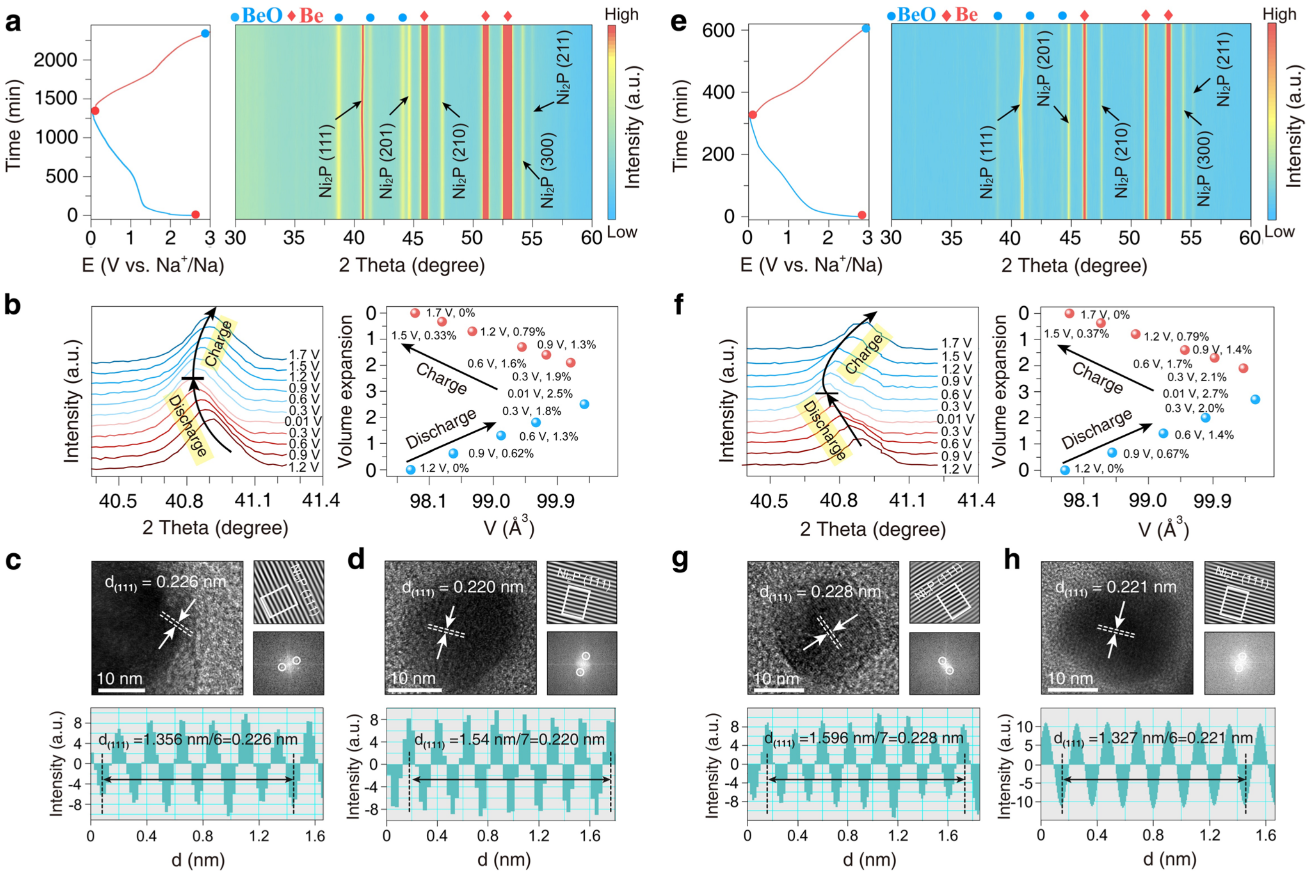

Fig. 4 In-situ and ex-situ structure evolution of Ni_2P@GPC/CFP during sodiation/desodiation. **a** Charge–discharge curve and curve and in-situ XRD patterns at the first cycle. **b** XRD of Ni_2P (111) and unit cell volume change during the first cycle. **c, d** HRTEM image and corresponding FFT of Ni_2P at 0.01 V (discharge) and 3.0 V (charge) in the first cycle. **e** Charge–discharge curve and in-situ XRD patterns at the 10th cycle. **f** Ni_2P (111) evolution and volume change during the 10th cycle. **g, h** HRTEM image and corresponding FFT of Ni_2P at 0.01 V (discharge) and 3.0 V (charge) in the 10th cycle

initial lattice expansion is more pronounced but becomes increasingly accommodated over cycles. Additionally, SEM–EDX mapping at different charge/discharge states after 10 cycles (Figs. S17-S19) shows uniform distributions of Ni, P, and C with no evidence of aggregation or phase separation, further supporting the intercalation-dominated, non-conversion behavior of Na^+ storage in Ni_2P.

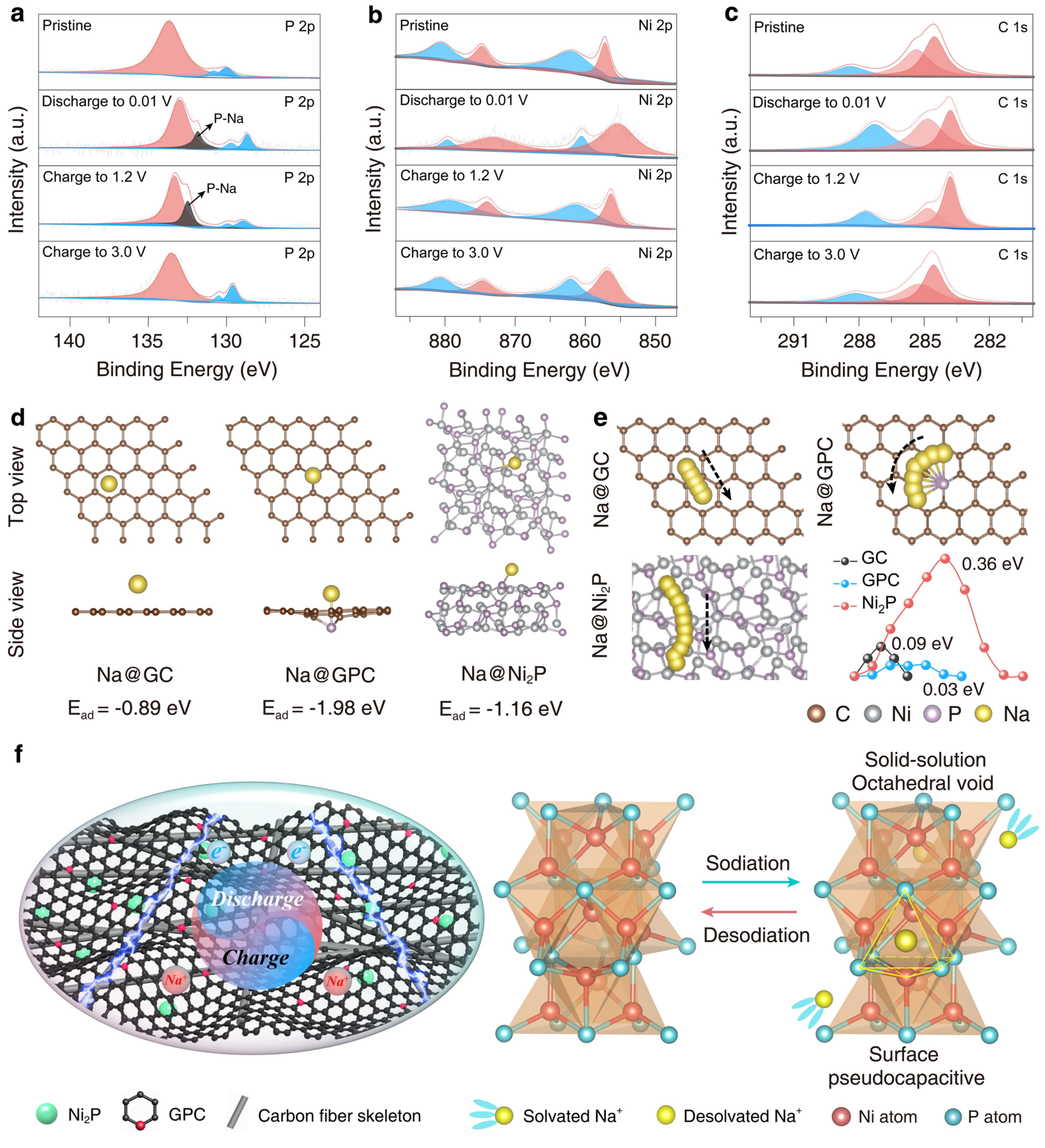

Fig. 5 **a–c** Ex-situ XPS analysis of P 2*p*, Ni 2*p* and C 1*s* at different sodiation/desodiation states. **d** Top and front views of Na^+ adsorption sites on the GC, GPC and Ni_2P surfaces, along with their corresponding adsorption energies. **e** Na^+ diffusion paths on GC, GPC and Ni_2P surfaces, together with the associated diffusion barriers. **f** Schematic illustration of the proposed sodium storage behavior for Ni_2P@GPC/CFP

Quasi-in-situ XPS further provides insights into the electronic evolution during Na^+ insertion/extraction. In the P 2*p* spectra (Fig. 5a), pristine Ni_2P@GPC/CFP displays characteristic P-Ni and P–C peaks. Upon discharging to 0.01 V, a new P-Na feature emerges, accompanied by a negative shift of the P-Ni peak, indicating increased electron density on P as Na^+ occupies interstitial sites to form Na_xNi_2P [66]. During charging, the P-Na signal weakens at 1.2 V and disappears at 3.0 V, with the P-Ni peaks returning to their initial positions, demonstrating excellent reversibility. The Ni 2*p* spectra (Fig. 5b) show parallel negative shifts during sodiation and recovery upon desodiation, confirming reversible electron redistribution around Ni without forming metallic Ni. Meanwhile, the C 1*s* spectra (Fig. 5c) reveal subtle shifts of C–C/C=C and C–O/C–P components upon discharge, which also recover after charging, suggesting a reversible modulation of the carbon scaffold and C-P bonding. These findings collectively demonstrate a fully reversible electronic environment, consistent with an intercalation-dominated solid-solution mechanism.

DFT calculations were also performed to provide atomic-level insights into Na^+ adsorption and diffusion (Fig. 5d). The calculated adsorption energies are -0.89, -1.98, and -1.16 eV on GC (001), GPC (001), and Ni_2P (111), respectively, indicating that heteroatom-doped porous carbon offers the most favorable adsorption sites, while Ni_2P also contributes strong anchoring. The corresponding diffusion barriers are 0.09, 0.03, and 0.36 eV for GC, GPC, and Ni_2P, respectively (Fig. 5e), suggesting that although Ni_2P affords strong Na binding, it suffers from sluggish ion transport. Compositing Ni_2P with conductive GPC therefore combines strong adsorption with ultrafast ion diffusion, reconciling capacity retention with high-rate performance.

Taken together, the structural, spectroscopic, and theoretical findings consistently demonstrate that Na^+ storage in Ni_2P@GPC/CFP occurs through an interstitial solid-solution mechanism, in which desolvated Na^+ ions enter and exit lattice interstitials along the (111) plane pathways without generating Na_3P or metallic Ni. Figure 5f illustrates the proposed sodium storage behavior for Ni_2P@GPC/CFP. This mechanism facilitates highly reversible lattice breathing and structural stabilization during cycling. In parallel, kinetics analyses (CV and GITT/EIS) demonstrate dominant pseudocapacitive contributions at higher rates, synergistically complementing the solid-solution process. The dual-mode storage mechanism, comprising solid-solution intercalation coupled with capacitive behavior, underpins the high rate capability, capacity retention, and long-term durability of Ni_2P@GPC/CFP.

4 Conclusions

In summary, we demonstrate a freestanding Ni_2P-based nanocomposite electrode that enables a dual-mode sodium-storage mechanism, conclusively identified as a cooperative interplay between interstitial solid-solution intercalation and surface pseudocapacitance. This concerted mechanism, which avoids the conventional conversion reaction, is facilitated by the designed hierarchical porosity and nanoconfinement, yielding high reversible specific capacity of ≈405 mAh g^{-1} after 300 cycles, outstanding rate capability (135 mAh g^{-1} at 10 A g^{-1}) and long-term stability with a specific capacity of 263 mAh g^{-1} at 1 A g^{-1} after 2000 cycles, corresponding to a capacity retention of 78.2%.

Acknowledgements This research was financially supported by the National Natural Science Foundation of China (52372187, 52394170, 52394171), the Fundamental Research Funds for the Central Universities of China (buctrc202503, JZ2024HGTG0291, PA2025GDSK0054), the Anhui Provincial Special Support Program for Innovative Leading Talents (Z2023TP0002), the Higher Education Discipline Innovation Project "New Materials and Technology for Clean Energy" (B18018), the "Transformational Technologies for Clean Energy and Demonstration" Strategic Priority Research Program of Chinese Academy of Sciences (Grant No. XDA21000000), the Anhui Provincial Natural Science Foundation (2408085MB029), and the Hefei Institute of Technology Talent Research Fund (2025KY41).

Author Contributions Jiaqin Liu helped in project administration, funding acquisition, and review. Tongzhen Wang and Jie Yang carried out software, investigation, and validation. Yulei Li helped in methodology, formal analysis, and writing—original draft writing. Zhaoqian Li and Jiewu Cui helped in writing—review & editing and visualization. Yan Yu and Yucheng Wu contributed to conceptualization, review, and supervision.

Declarations

Conflict of interest The authors declare no interest conflict. They have no known competing financial interests or personal relationships that could have appeared to influence the work reported in this paper.

Supplementary Information The online version contains supplementary material available at https://doi.org/10.1007/s40820-026-02076-0.

References

1. S. Gan, Y. Huang, N. Hong, Y. Zhang, B. Xiong et al., Comprehensive understanding of closed pores in hard carbon anode for high-energy sodium-ion batteries. Nano-Micro Lett. **17**(1), 325 (2025). https://doi.org/10.1007/s40820-025-01833-x
2. Y. Gao, Q. Yu, H. Yang, J. Zhang, W. Wang, The enormous potential of sodium/potassium-ion batteries as the mainstream energy storage technology for large-scale commercial applications. Adv. Mater. **36**(39), 2405989 (2024). https://doi.org/10.1002/adma.202405989
3. H. Yang, D. Wang, Y. Liu, Y. Liu, B. Zhong et al., Improvement of cycle life for layered oxide cathodes in sodium-ion batteries. Energy Environ. Sci. **17**(5), 1756–1780 (2024). https://doi.org/10.1039/D3EE02934D
4. Z. Lin, Y. Cai, S. Zhang, J. Sun, Y. Liu et al., Wide-temperature electrolytes for aqueous alkali metal-ion batteries: challenges, progress, and prospects. Nano-Micro Lett. **18**(1), 27 (2025). https://doi.org/10.1007/s40820-025-01865-3
5. M. Wang, H. Zhang, B. Song, W. Zhang, E. Zhang et al., Sandwiched MnO_2-$Fe(CN)_6^{4-}$-doped PPy-MnO_2 cathodes with tunable interlayer spaces and dual redox active sites for enhanced Na storage. Ind. Eng. Chem. Res. **63**(21), 9600–9608 (2024). https://doi.org/10.1021/acs.iecr.4c00969
6. P. Liang, D. Pan, X. Hu, K.R. Yang, Y. Liu et al., Se-regulated MnS porous nanocubes encapsulated in carbon nanofibers as high-performance anode for sodium-ion batteries. Nano-Micro Lett. **17**(1), 237 (2025). https://doi.org/10.1007/s40820-025-01767-4
7. X. Zhang, H. Qu, W. Yan, L. Yang, Y. Li et al., Sodium-based dual-ion battery: from materials to mechanism. Angew. Chem. Int. Ed. **64**(48), e202510566 (2025). https://doi.org/10.1002/anie.202510566
8. B. Pei, H. Yu, L. Zhang, G. Fang, J. Zhou et al., Hard carbon for sodium-ion batteries: from fundamental research to practical applications. Adv. Mater. **37**(39), e2504574 (2025). https://doi.org/10.1002/adma.202504574
9. X. Man, X. Min, Y. Yan, H. Gong, Y. Dai et al., Prospect of bismuth and its compounds in sodium-ion batteries: a review. Energy Storage Mater. **75**, 104076 (2025). https://doi.org/10.1016/j.ensm.2025.104076
10. Y. Liu, W. Zhou, S. Jiang, S. Song, Regulating cocatalyst spin-electronic structures for achieving solar-to-H_2 of 7.32% in photothermal-catalytic H_2O overall splitting. Small **21**(41), e08219 (2025). https://doi.org/10.1002/smll.202508219
11. L. Wang, Q. Li, Z. Chen, Y. Wang, Y. Li et al., Metal phosphide anodes in sodium-ion batteries: latest applications and progress. Small **20**(26), 2310426 (2024). https://doi.org/10.1002/smll.202310426
12. J. Liang, G. Zhu, Y. Zhang, H. Liang, W. Huang, Conversion of hydroxide into carbon-coated phosphide using plasma for sodium ion batteries. Nano Res. **15**(3), 2023–2029 (2022). https://doi.org/10.1007/s12274-021-3738-8
13. M. Ishaq, M. Jabeen, R. Haider, K. Nadir, F. Ilyas et al., Geometric design and electronic engineering of transition metal phosphides for key electrochemical energy technologies: nanoarchitectonics and application. Adv. Funct. Mater. **35**(37), 2424141 (2025). https://doi.org/10.1002/adfm.202424141
14. S. Liu, Q. Shi, X. Liu, M. Zhang, F. Lin et al., Rational tailoring the hetero-architectures of Ni_2P/CoP_2 for stable and high-power sodium-ion batteries. J. Energy Storage **126**, 117026 (2025). https://doi.org/10.1016/j.est.2025.117026
15. C. Dong, L. Guo, Y. He, C. Chen, Y. Qian et al., Sandwich-like Ni_2P nanoarray/nitrogen-doped graphene nanoarchitecture as a high-performance anode for sodium and lithium ion batteries. Energy Storage Mater. **15**, 234–241 (2018). https://doi.org/10.1016/j.ensm.2018.04.011
16. F. Wang, T. Zhang, T. Zhang, T. He, F. Ran, Recent progress in improving rate performance of cellulose-derived carbon materials for sodium-ion batteries. Nano-Micro Lett. **16**(1), 148 (2024). https://doi.org/10.1007/s40820-024-01351-2
17. H. Wu, S. Luo, H. Wang, L. Li, Y. Fang et al., A review of anode materials for dual-ion batteries. Nano-Micro Lett. **16**(1), 252 (2024). https://doi.org/10.1007/s40820-024-01470-w
18. Y. Hao, J. Shao, Y. Yuan, X. Li, W. Xiao et al., Design of phosphide anodes harvesting superior sodium storage: progress, challenges, and perspectives. Adv. Funct. Mater. **33**(13), 2212692 (2023). https://doi.org/10.1002/adfm.202212692
19. Q. Zheng, S. Zhou, S. Tang, H. Zeng, Y. Tang et al., Unveiling atom migration abilities affected anode performance of sodium-ion batteries. Angew. Chem. Int. Ed. **62**(27), e202303343 (2023). https://doi.org/10.1002/anie.202303343
20. S. Liu, Q. Shi, X. Liu, J. Fan, L. Ren et al., Ni_2P /Cu_3P bimetallic phosphide embedded in nitrogen-doped carbon as SIB anode: constructed hetero interface promoting fast Na^+ diffusion and storage performance. Chem. Eng. J. **502**, 157889 (2024). https://doi.org/10.1016/j.cej.2024.157889
21. M. Zhang, Y. Liang, F. Liu, X. An, J. Feng et al., Ni_2P immobilized on N, P-codoped porous carbon sheets for alkali metal ion batteries and storage mechanism. J. Mater. Chem. A **11**(15), 8162–8172 (2023). https://doi.org/10.1039/D2TA09890C
22. H. Wu, G. Xia, X. Yu, Unlocking the potential of iron sulfides for sodium-ion batteries by ultrafine pulverization. Small **20**(32), 2312190 (2024). https://doi.org/10.1002/smll.202312190

23. J. Li, X. Chang, T. Huang, B. Wang, H. Zheng et al., Surface-controlled sodium-ion storage mechanism of $Li_4Ti_5O_{12}$ anode. Energy Storage Mater. **54**, 724–731 (2023). https://doi.org/10.1016/j.ensm.2022.11.017
24. T. Li, D. Zhao, M. Shi, C. Tian, J. Yi et al., Quantum-size FeS_2 with delocalized electronic regions enable high-performance sodium-ion batteries across wide temperatures. Nano-Micro Lett. **18**(1), 15 (2025). https://doi.org/10.1007/s40820-025-01858-2
25. D.D. Robertson, H. Cumberbatch, D.J. Pe, Y. Yao, S.H. Tolbert, Understanding how the suppression of insertion-induced phase transitions leads to fast charging in nanoscale Li_xMoO_2. ACS Nano **18**(1), 996–1012 (2024). https://doi.org/10.1021/acsnano.3c10169
26. Z. Yan, D. Tang, S. Fan, X. Zou, X. Huang et al., Unifying electrochemically-driven multistep phase transformations of rutile TiO_2 to rocksalt nanograins for reversible Li^+ and Na^+ storage. Adv. Mater. **37**(11), e2419999 (2025). https://doi.org/10.1002/adma.202419999
27. Y. Yun, B. Xi, F. Tian, W. Chen, W. Sun et al., Zero-strain structure for efficient potassium storage: nitrogen-enriched carbon dual-confinement CoP composite. Adv. Energy Mater. **12**(3), 2103341 (2022). https://doi.org/10.1002/aenm.202103341
28. J. Zhang, G. Kim, M. Park, J. Zhang, S. Lee et al., Nanostructuring-promoted non-equilibrium phase transformation of Bi anodes toward diffusion-controlled reaction for K-ion batteries. Adv. Energy Mater. **12**(48), 2202446 (2022). https://doi.org/10.1002/aenm.202202446
29. X. Zou, Z. Yan, D. Tang, S. Fan, D.-L. Peng et al., Intercalation pseudocapacitance of sodium-ion storage in TiO_2(B). J. Mater. Chem. A **12**(23), 13770–13777 (2024). https://doi.org/10.1039/D4TA02211D
30. Q. Wei, X. Chang, D. Butts, R. DeBlock, K. Lan et al., Surface-redox sodium-ion storage in anatase titanium oxide. Nat. Commun. **14**(1), 7 (2023). https://doi.org/10.1038/s41467-022-35617-3
31. Y. Yao, H. Cumberbatch, D.D. Robertson, M.A. Chin, R. Lamkin et al., On the interplay between size and disorder in suppressing intercalation-induced phase transitions in pseudocapacitive nanostructured MoS_2. Adv. Funct. Mater. **34**(50), 2304896 (2024). https://doi.org/10.1002/adfm.202304896
32. Z. Zeng, B.-A. Mei, G. Song, M. Hamza, Z. Yan et al., Physical interpretation of the electrochemical impedance spectroscopy (EIS) characteristics for diffusion-controlled intercalation and surface-redox charge storage behaviors. J. Energy Storage **102**, 114021 (2024). https://doi.org/10.1016/j.est.2024.114021
33. Z. Zhao, Y. Wu, R. Hu, J. Lu, D. Chen et al., Intercalation pseudocapacitance in 2D $VS_2/Ti_3C_2T_x$ MXene hybrids for all-climate and long-cycle sodium-ion batteries. Adv. Funct. Mater. **33**(50), 2307794 (2023). https://doi.org/10.1002/adfm.202307794
34. W. Meng, Z. Dang, D. Li, L. Jiang, D. Fang, Interface and defect engineered titanium-base oxide heterostructures synchronizing high-rate and ultrastable sodium storage. Adv. Energy Mater. **12**(40), 2201531 (2022). https://doi.org/10.1002/aenm.202201531
35. Z. Guo, Z. Xu, F. Xie, J. Jiang, K. Zheng et al., Investigating the superior performance of hard carbon anodes in sodium-ion compared with lithium- and potassium-ion batteries. Adv. Mater. **35**(42), 2304091 (2023). https://doi.org/10.1002/adma.202304091
36. H. Gao, W. Gao, M. Pumera, 3D-printed nanostructured copper substrate boosts the sodiated capability and stability of antimony anode for sodium-ion batteries. Adv. Funct. Mater. **34**(19), 2310563 (2024). https://doi.org/10.1002/adfm.202310563
37. G. Kresse, J. Furthmüller, Efficiency of ab-initio total energy calculations for metals and semiconductors using a plane-wave basis set. Comput. Mater. Sci. **6**(1), 15–50 (1996). https://doi.org/10.1016/0927-0256(96)00008-0
38. G. Kresse, J. Furthmüller, Efficient iterative schemes for *ab initio* total-energy calculations using a plane-wave basis set. Phys. Rev. B **54**(16), 11169–11186 (1996). https://doi.org/10.1103/physrevb.54.11169
39. J.D. Pack, H.J. Monkhorst, Special points for Brillouin-zone integrations": a reply. Phys. Rev. B **16**(4), 1748–1749 (1977). https://doi.org/10.1103/physrevb.16.1748
40. L. Yang, H. Pang, W. Ren, X. Wang, Y. Wei et al., Joule heating driven graphitization regulation and Ni single-atom modification in hard carbon for low-voltage and high-rate potassium-ion storage. Adv. Funct. Mater. e16237 (2025). https://doi.org/10.1002/adfm.202516237
41. A.K. Nandi, D.P. Chatterjee, Hybrid polymer gels for energy applications. J. Mater. Chem. A **11**(24), 12593–12642 (2023). https://doi.org/10.1039/d2ta09525d
42. Y. Zhao, W.-J. Jiang, J. Zhang, E.C. Lovell, R. Amal et al., Anchoring sites engineering in single-atom catalysts for highly efficient electrochemical energy conversion reactions. Adv. Mater. **33**(41), 2102801 (2021). https://doi.org/10.1002/adma.202102801
43. G. Wu, X. Wu, X. Zhu, J. Xu, N. Bao, Two-dimensional hybrid nanosheet-based supercapacitors: from building block architecture, fiber assembly, and fabric construction to wearable applications. ACS Nano **16**(7), 10130–10155 (2022). https://doi.org/10.1021/acsnano.2c02841
44. D. Liu, J. Ma, S. Zheng, W. Shao, T. Zhang et al., High-performance and flexible co-planar integrated microsystem of carbon-based all-solid-state micro-supercapacitor and real-time temperature sensor. Energy Environ. Mater. **6**(6), e12445 (2023). https://doi.org/10.1002/eem2.12445
45. Y. Liu, J. Wang, Q. Shi, M. Yan, S. Zhao et al., A stress self-adaptive structure to suppress the chemo-mechanical degradation for high rate and ultralong cycle life sodium ion batteries. Angew. Chem. Int. Ed. **62**(29), e202303875 (2023). https://doi.org/10.1002/anie.202303875
46. X. Cui, J. Chen, Z. Sun, L. Wang, Q. Peng et al., A general route for encapsulating monodispersed transition metal phosphides into carbon multi-chambers toward high-efficient lithium-ion storage with underlying mechanism exploration. Adv. Funct.

Mater. **33**(15), 2212100 (2023). https://doi.org/10.1002/adfm.202212100

47. D. Li, Z. Li, R. Zou, G. Shi, Y. Huang et al., Coupling overall water splitting and biomass oxidation *via* Fe-doped Ni_2P@C nanosheets at large current density. Appl. Catal. B Environ. Energy **307**, 121170 (2022). https://doi.org/10.1016/j.apcatb.2022.121170
48. Y. Liang, N. Song, Z. Zhang, W. Chen, J. Feng et al., Integrating Bi@C nanospheres in porous hard carbon frameworks for ultrafast sodium storage. Adv. Mater. **34**(28), 2202673 (2022). https://doi.org/10.1002/adma.202202673
49. J. Xiao, Z. Cai, T. Muhmood, X. Hu, S. Lin, Tailoring ordered porous carbon embedded with Cu clusters for high-energy and long-lasting phosphorus anode. Small **18**(11), 2106930 (2022). https://doi.org/10.1002/smll.202106930
50. J. Bai, J.H. Jia, Y. Wang, C.C. Yang, Q. Jiang, Ideal bi-based hybrid anode material for ultrafast charging of sodium-ion batteries at extremely low temperatures. Nano-Micro Lett. **17**(1), 60 (2024). https://doi.org/10.1007/s40820-024-01560-9
51. H. Zhang, W. Liu, Z. Li, L. Qiao, K. Chi et al., Constructing CoP/Ni_2P heterostructure confined Ru sub-nanoclusters for enhanced water splitting in wide pH conditions. Adv. Sci. **11**(35), 2401398 (2024). https://doi.org/10.1002/advs.202401398
52. Y. Liao, Y. Chen, L. Li, S. Luo, Y. Qing et al., Ultrafine homologous Ni_2P–Co_2P heterostructures *via* space-confined topological transformation for superior urea electrolysis. Adv. Funct. Mater. **33**(42), 2303300 (2023). https://doi.org/10.1002/adfm.202303300
53. J. Yuan, T. Sun, J. Chen, R. Zhou, J. Cao et al., Microbial surface confined growth strategy for the synthesis of highly loaded NiCoP nanoparticles with hollow derived carbon shells for sodium ion capture. Adv. Sci. **12**(1), 2407616 (2025). https://doi.org/10.1002/advs.202407616
54. H. Feng, Z. Liu, F. Wang, L. Xue, L. Li et al., The C─S/C═S bonds synergistically modify porous hollow-carbon-nanocages anode for durable and fast sodium-ion storage. Adv. Funct. Mater. **34**(33), 2400020 (2024). https://doi.org/10.1002/adfm.202400020
55. C. Ding, S. Li, S. Yin, X. Zeng, W. Wang et al., Rationally designed Ni_2P/C composite membrane with enhanced electrochemical reversibility and stability for lithium-ion storage. J. Power. Sources **579**, 233300 (2023). https://doi.org/10.1016/j.jpowsour.2023.233300
56. L. Li, A. Huang, H. Jiang, Y. Li, X. Pan et al., Encapsulation of Sn sub-nanoclusters in multichannel carbon matrix for high-performance potassium-ion batteries. Angew. Chem. Int. Ed. **63**(45), e202412077 (2024). https://doi.org/10.1002/anie.202412077
57. Y. Yang, J. Xia, X. Guan, Z. Wei, J. Yu et al., In situ growth of CoP nanosheet arrays on carbon cloth as binder-free electrode for high-performance flexible lithium-ion batteries. Small **18**(51), 2204970 (2022). https://doi.org/10.1002/smll.202204970
58. J. Yu, Y. He, J. Li, C. Dong, Y. Dai et al., In-situ rooting biconical-nanorods-like Co-doped FeP @carbon architectures toward enhanced lithium storage performance. Chem. Eng. J. **477**, 146996 (2023). https://doi.org/10.1016/j.cej.2023.146996
59. S. Lin, H. Zhang, C. Shu, W. Hua, X. Wang et al., Research progress and perspectives on pre-sodiation strategies for sodium-ion batteries. Adv. Funct. Mater. **34**(51), 2409628 (2024). https://doi.org/10.1002/adfm.202409628
60. J. Zong, Y. Liang, F. Liu, M. Zhang, J. Feng et al., Effect of combination model of $MoTe_2$ and MXene layers on sodium ion storage. Adv. Mater. **37**(34), 2503252 (2025). https://doi.org/10.1002/adma.202503252
61. Q. Wei, Q. Li, Y. Jiang, Y. Zhao, S. Tan et al., High-energy and high-power pseudocapacitor-battery hybrid sodium-ion capacitor with Na^+ intercalation pseudocapacitance anode. Nano-Micro Lett. **13**(1), 55 (2021). https://doi.org/10.1007/s40820-020-00567-2
62. R. Yang, X. Qiu, H. Xiong, Z. Cui, Y. Xue et al., Growth space engineering of closed pores in hard carbon for low-temperature sodium-ion batteries. Energy Storage Mater. **80**, 104415 (2025). https://doi.org/10.1016/j.ensm.2025.104415
63. P. Song, J. Yang, C. Wang, T. Wang, H. Gao et al., Interface engineering of Fe_7S_8/FeS_2 heterostructure in situ encapsulated into nitrogen-doped carbon nanotubes for high power sodium-ion batteries. Nano-Micro Lett. **15**(1), 118 (2023). https://doi.org/10.1007/s40820-023-01082-w
64. C. Chen, Y. Tian, R. Ren, S. Duan, D. Wang et al., Regulating pores and carbonyl groups of biomass-derived hard carbon for enhanced sodium storage. Adv. Sci. **12**(40), e10328 (2025). https://doi.org/10.1002/advs.202510328
65. M. Li, R. Li, H. Ma, M. Yang, Y. Dai et al., An ultra-stable, high-energy and wide-temperature-range aqueous alkaline sodium-ion battery with the microporous C_4N/rGO anode. Nano-Micro Lett. **17**(1), 158 (2025). https://doi.org/10.1007/s40820-024-01589-w
66. L. Wang, B. Liu, Y. Zhu, M. Yang, C. Du et al., General metal–organic framework-derived strategy to synthesize yolk-shell carbon-encapsulated nickelic spheres for sodium-ion batteries. J. Colloid Interface Sci. **613**, 23–34 (2022). https://doi.org/10.1016/j.jcis.2021.12.157